

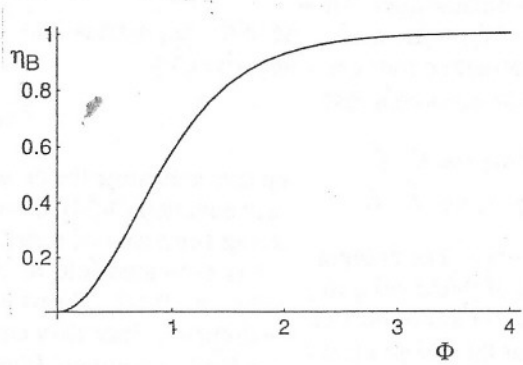
$$\eta_B = e^{-4\Phi_a'} \sinh^2(\sqrt{\Phi_a'})$$

$$\Phi_a' = 0.55 \Rightarrow \eta_{B,MAX} = 0.037$$

**FIGURE 9.32**  
Maximum possible Bragg matched diffraction efficiency vs.  $\Phi_a'$  for a thick amplitude transmission grating.

**FIGURE 9.33**  
Diffraction efficiency of a thick amplitude transmission grating with Bragg mismatch.

$$\Phi_a' = \alpha_0 d / 2 \cos \theta$$



$$\eta_B = \tanh^2 \Phi$$

$$\eta_{B,MAX} = 1$$

**FIGURE 9.34**  
Diffraction efficiency of a thick Bragg matched phase reflection grating.

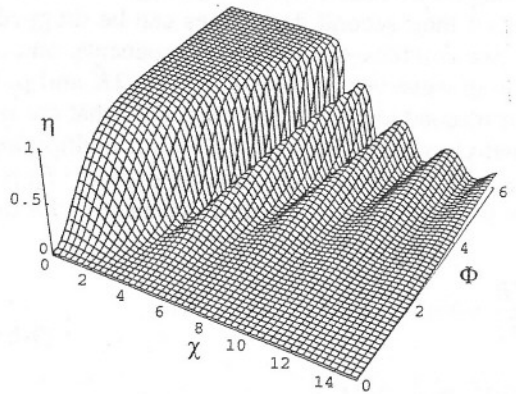
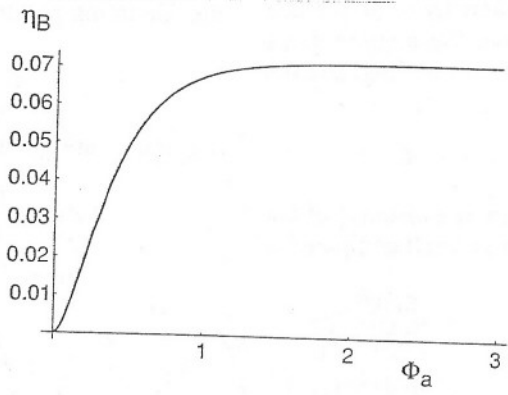


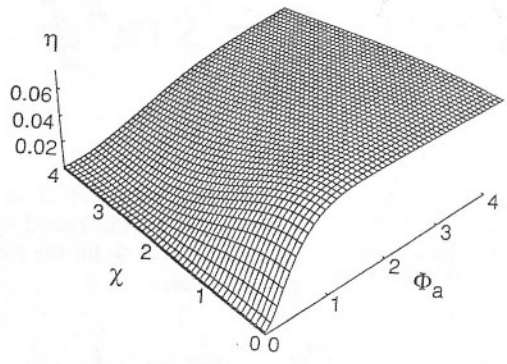
**FIGURE 9.35**  
Diffraction efficiency of a thick phase reflection grating when Bragg mismatch is present.

$$\Phi_a = \frac{\alpha_1 d}{2 \cos \theta}$$



$$\eta_B = \left[ 2 + \sqrt{3} \coth(\sqrt{3} \Phi_a) \right]^{-2}$$

**FIGURE 9.36**  
Bragg matched diffraction efficiency of thick amplitude reflection grating.



$$\Phi_a \rightarrow \infty \Rightarrow \eta_{B,MAX} = 0.072$$

**FIGURE 9.37**  
Diffraction efficiency of a thick amplitude hologram when Bragg mismatch is present.

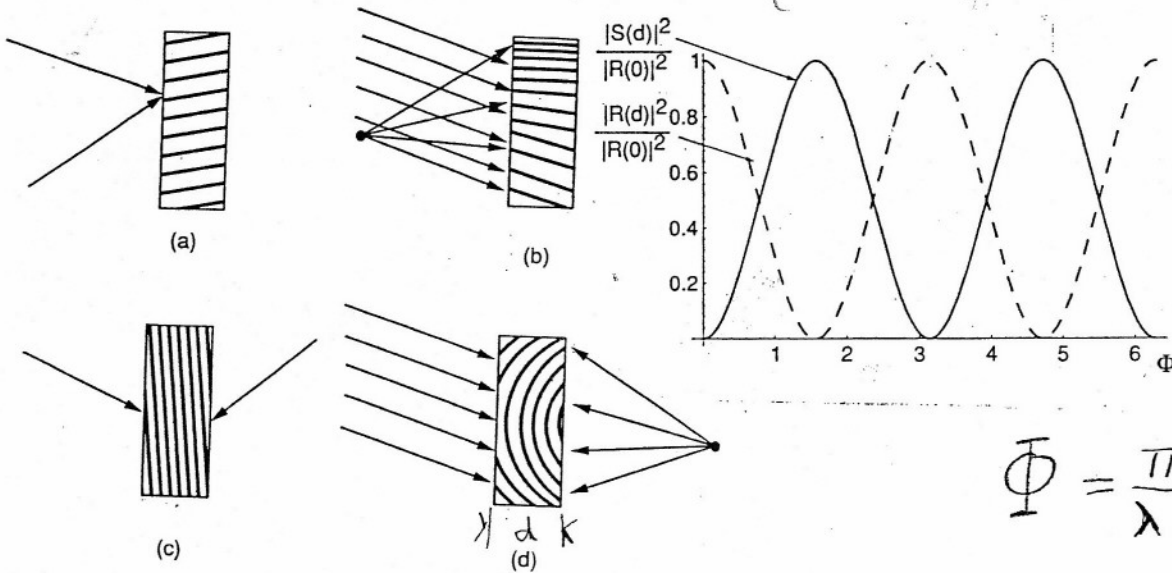


**FIGURE 9.26**  
 Orientation of interference fringes within a recording medium. (a) Two plane waves forming slant fringes, (b) a plane wave and a spherical wave, (c) two plane waves impinging from opposite sides of the emulsion, and (d) a plane wave and a spherical wave impinging from opposite sides of the recording medium.

$$\eta = \sin^2 \Phi$$

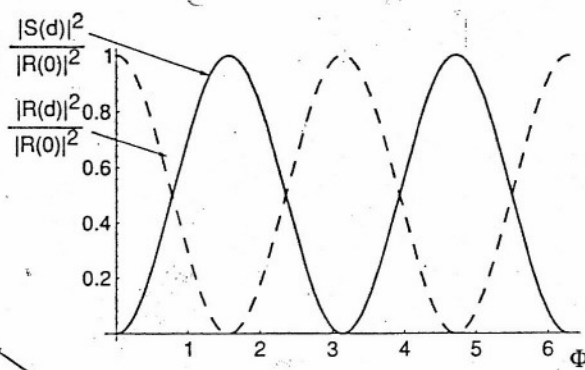


**FIGURE 9.30**  
 Normalized intensities of the diffracted and undiffracted wave as a function of  $\Phi$  for the Bragg matched case.

$$\Phi = \frac{\pi \Delta n_{mx} d}{\lambda \cos \theta}$$

$$\chi = \frac{\pi d}{\lambda \cos \theta} \left[ \Delta \theta \cos \theta - \frac{\Delta \lambda}{\lambda} \right]$$

$$n = n_0 + \Delta n \cos(\vec{k}_g \cdot \vec{r})$$

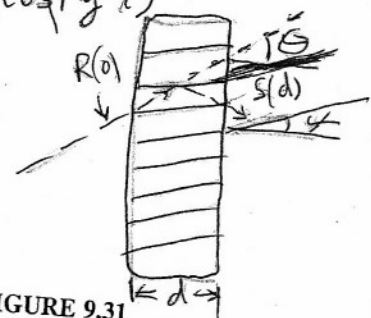
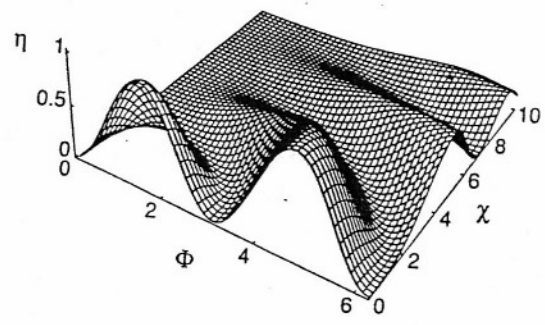


**FIGURE 9.31**  
 Diffraction efficiency of a thick phase transmission grating when Bragg mismatch is present.

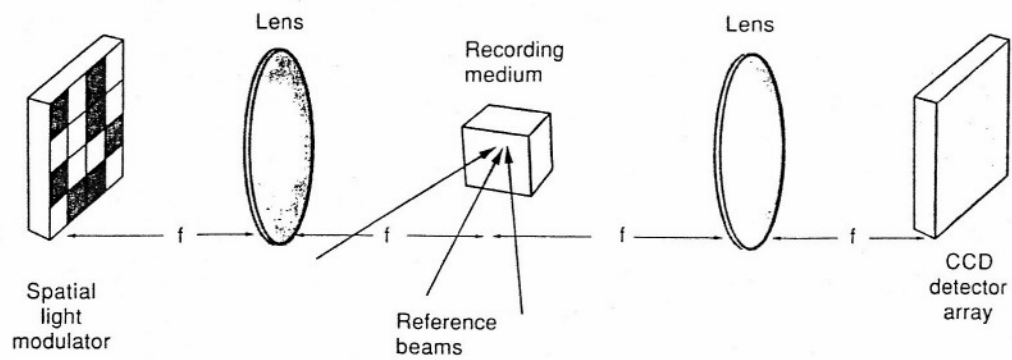


**FIGURE 9.57**  
 A volume holographic storage system. The case of angle multiplexing is illustrated.

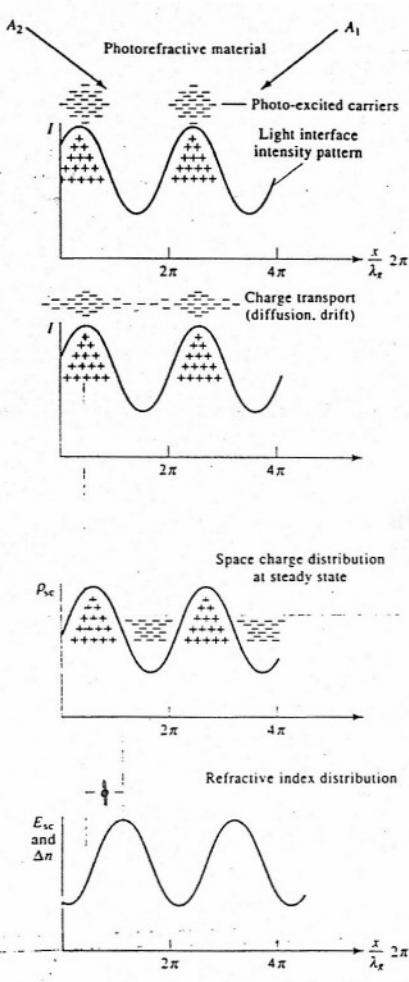


Figure 18-2 The photorefractive mechanism. Two coherent light beams intersect in an electrooptic crystal, forming an interference pattern. Electrons are excited where the intensity is large and migrate to regions of low intensity. The electric field associated with the resultant space charge operates through the electrooptic effect to produce a refractive index grating.  $\phi$  is the phase shift (in radians) between the light interference pattern and the index grating.

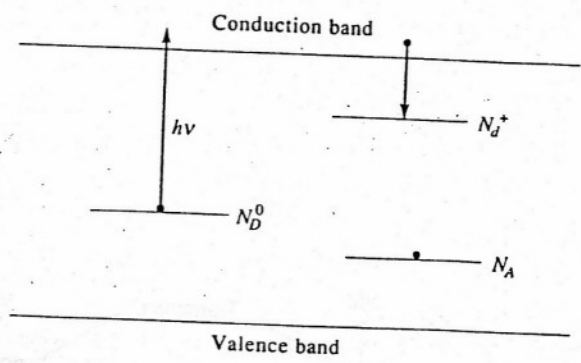


Figure 18-3 The deep impurity levels involved in the charge migration and trapping of a photorefractive crystal.

Handwritten equations:

$$\nabla \cdot \vec{E} = \frac{\rho_{sc}}{\epsilon}$$

$$E_{sc} = \int \frac{\rho_{sc}}{\epsilon} dx$$

$$\Delta n = \frac{1}{2} n_0^3 r_e E_{sc}$$

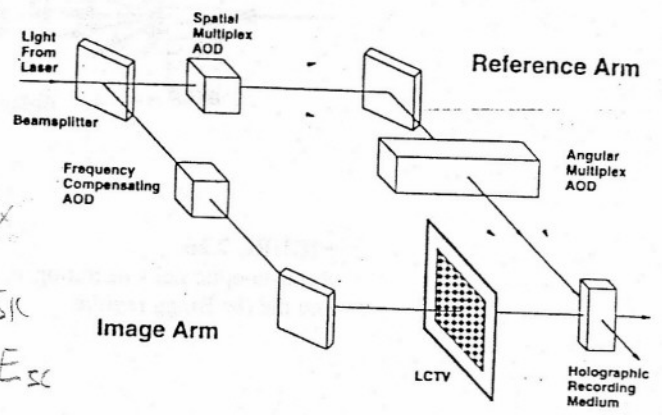


Fig. 11 Holographic memory demonstrator system layout.

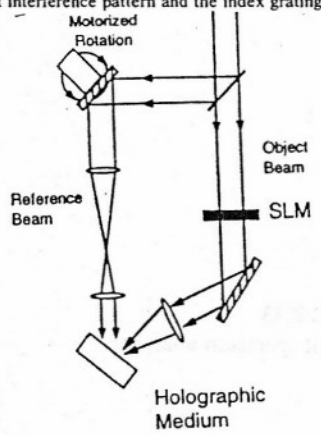


Fig. 7 Simplified angularly multiplexed storage system.

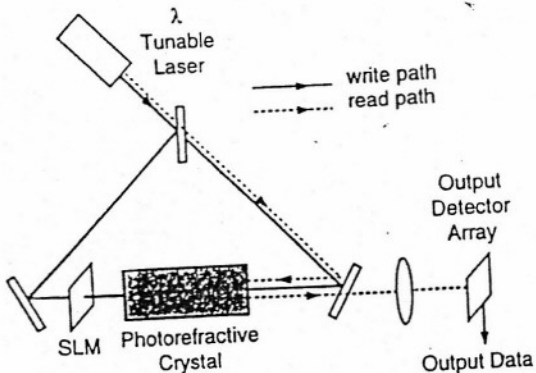
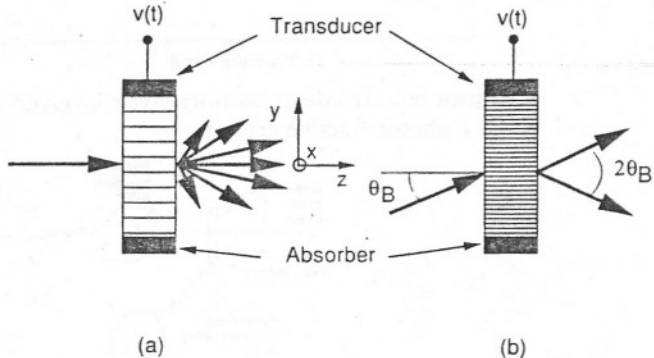
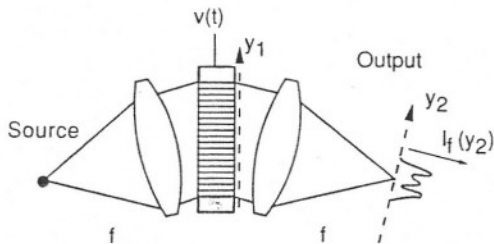


Fig. 9 Simplified wavelength multiplexed storage system.



**FIGURE 7.26**  
Acousto-optic cells operating in the (a) Raman-Nath regime and the (b) Bragg regime.



**FIGURE 8.33**  
Bragg cell spectrum analyzer.

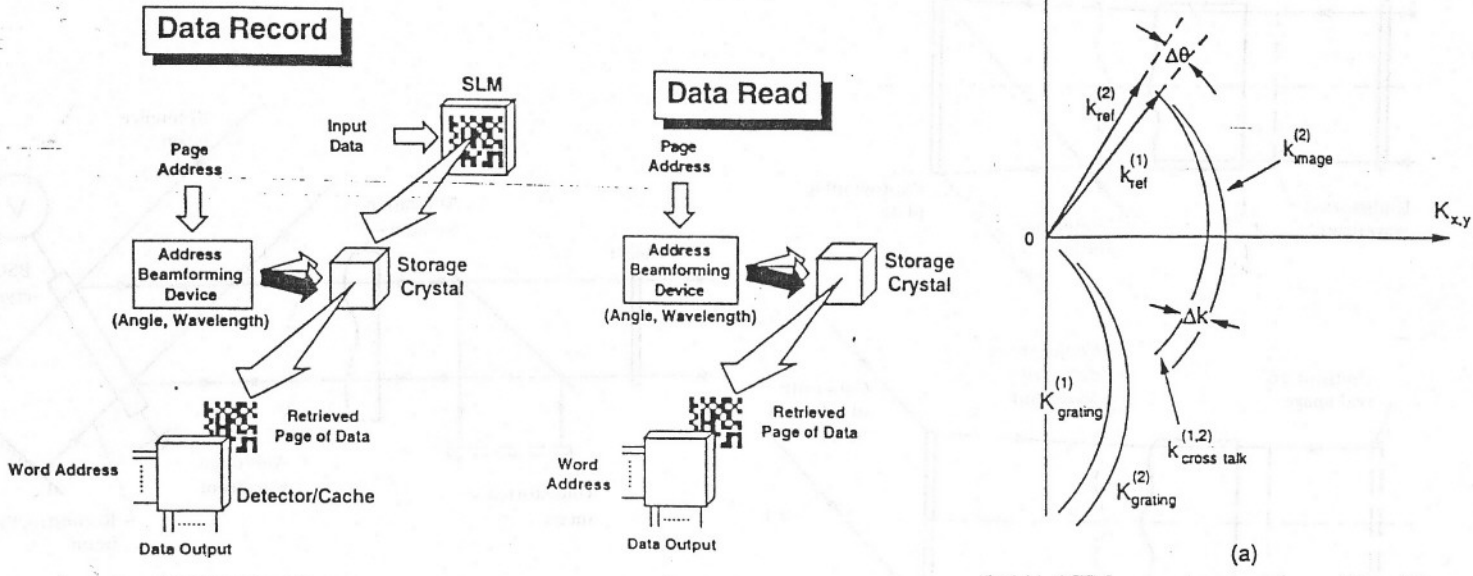


Fig. 1 Simplified system diagram of holographic mass memory.

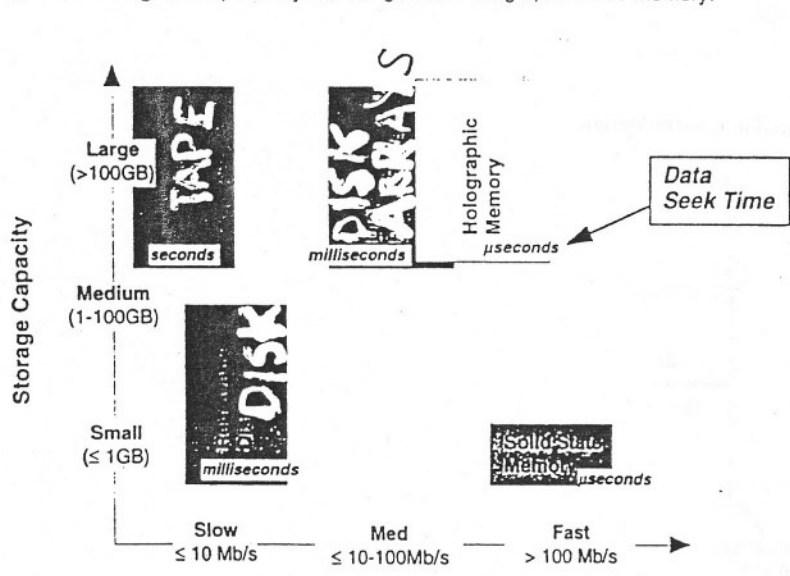


Fig. 2 Data storage technology spectrum.

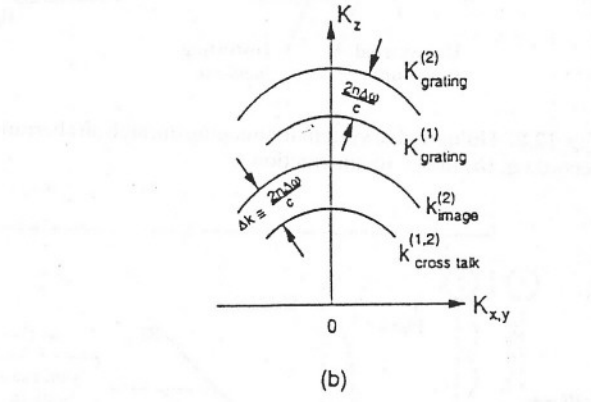


Figure 1-2. K space diagrams for volume holography using (a) angle-multiplexing scheme, (b) orthogonal multiplexing scheme

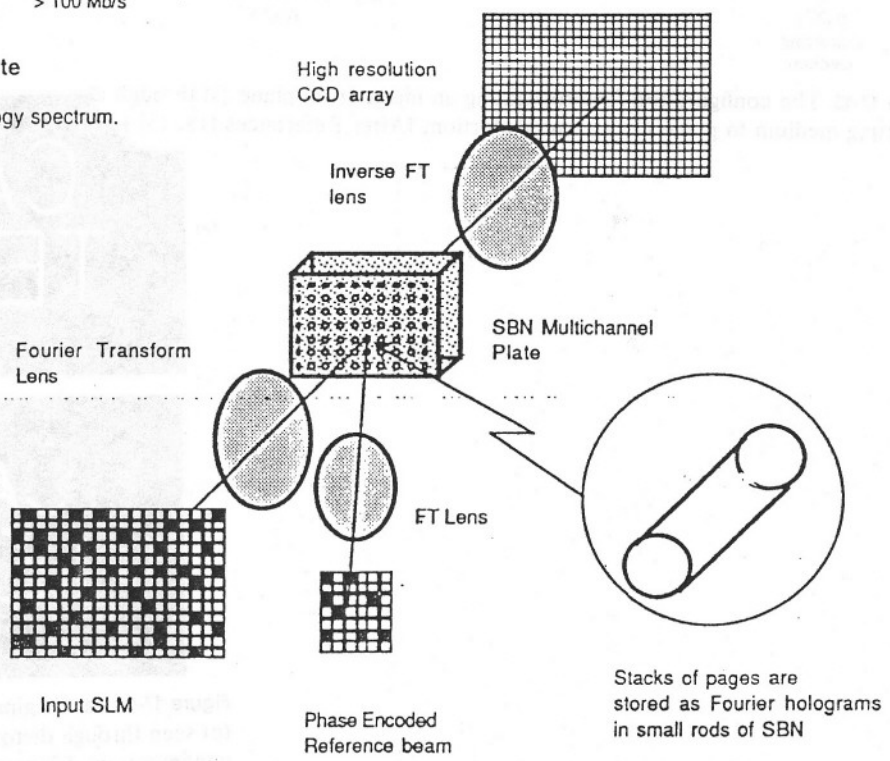


Figure 1 Schematic of a high-density, high-bandwidth data storage architecture.

